

# Towards Real-time Control of a CartPole System on a Quantum Computer

Nguyen Truong Thu Ngo<sup>1,2,†,\*</sup>, Vainö Mehtola<sup>3,†,\*</sup>, Jérôme Lenssen<sup>3</sup>, Peiyong Wang<sup>2,\*</sup>,  
 Francesco Cosco<sup>3</sup>, Tien-Fu Lu<sup>1</sup>, and James Q. Quach<sup>2,\*</sup>

<sup>1</sup>School of Electrical and Mechanical Engineering, Adelaide University, Adelaide, Australia

<sup>2</sup>Commonwealth Scientific and Industrial Research Organisation (CSIRO), Clayton, Victoria 3168, Australia

<sup>3</sup>VTT Technical Research Centre, Espoo, Finland

†These authors contributed equally and share first authorship.

\*Author to whom any correspondence should be addressed.

**E-mail:** nguyentruongthu.ngo@adelaide.edu.au, vaino.mehtola@vtt.fi, james.quach@csiro.au

**Keywords:** quantum reinforcement learning, robotics, quantum machine learning, NISQ, real-time control

## Abstract

The application of quantum reinforcement learning (QRL) to real-time control systems faces significant challenges regarding hardware latency, noise susceptibility, and learning convergence. This work presents an end-to-end investigation of a minimal hybrid quantum-classical agent applied to the CartPole benchmark, addressing the gap between idealized simulation and execution on a physical superconducting quantum processing unit (QPU). We demonstrate that a single-qubit agent acts as an effective learning model, solving the environment in substantially fewer episodes than a comparable classical actor-critic network even when the training of the hybrid agent is restricted to use parameter-shift for its quantum circuit component. To connect learning to deployment constraints, we map the inference-time trade-off between control-loop rate and measurement shot budget to provide guidance for an eventual real-time control demonstration. The resulting performance matrices show that both inference control frequency and shot count strongly affect balancing stability: higher inference frequencies consistently improve performance, and increasing the shot budget lowers the minimum inference frequency required to achieve near-maximal balancing. These results highlight the importance of finding an optimal medium between shot count and control frequency and developing circuits that are e.g. initial-state invariant. Lastly, we address the critical bottleneck of control latency on NISQ hardware. By bypassing the standard high-level software stack and programming the Zurich Instruments readout electronics directly via command tables, we achieve more than an order-of-magnitude improvement in execution speed on the VTT Q5 processor. These results quantify some of the current boundaries of quantum-assisted control and provide a start for achieving the tens-of-hertz throughput required for real-time closed-loop control feedback.

## 1 Introduction

Quantum machine learning (QML) investigates how quantum information processing can be leveraged for learning tasks, motivated by the fact that quantum systems can naturally represent and manipulate high-dimensional structures that are classically intractable [1–3]. From a theoretical perspective, several works have identified learning settings in which quantum models admit provable advantages over classical approaches, typically under complexity-theoretic or cryptographic assumptions [3–5]. While these results establish an important conceptual foundation for QML, they are often derived in idealized regimes and do not directly translate to near-term hardware nor practical applications. As a result, practical QML research has largely focused on hybrid algorithms compatible with noisy intermediate-scale quantum devices, where quantum circuits are embedded within classical optimization loops [6–8]. This paradigm is most commonly realized through parameterized quantum circuits (PQCs), in which gate parameters are treated as tunable variables that can encode classical data and be optimized using classical gradient-based or gradient-free methods [9, 10].

Reinforcement learning (RL) is a general framework for learning sequential decision-making policies from interaction with an environment, and it has become a standard methodology for, e.g., control and robotics when accurate system models are unavailable or difficult to derive [11–15]. Beyond continuous-control benchmarks, RL has demonstrated high-profile successes in complex

domains that require long-horizon planning and reliable generalization, including self-play systems that achieve superhuman performance in chess and the board game of shogi [16], large-scale agents for real-time strategy video games such as StarCraft II [17], and learned controllers for challenging robotic locomotion tasks [18]. Despite its successes, RL methods can remain sample-inefficient and exhibit sensitive training dynamics as problem dimensionality grows, and policies may lose performance when deployed under conditions that differ from those encountered during training.

Quantum reinforcement learning (QRL), a subfield of QML, applies quantum computing methods to reinforcement learning with the aim of improving aspects such as sample efficiency, exploration–exploitation trade-offs, and parameter count relative to fully classical approaches [19–24]. While there are no proven theoretical guarantees for QRL providing advantages over classical methods to date, prior work has focused on providing experimental results where QRL performs well in sample efficiency or parameter count [19, 21–31]. For the algorithms themselves, while primitive-based QRL approaches have been studied for improving sample efficiency, such as in the Grover-based works in [19, 21–24], more general PQC-based QRL has been explored in the context of the near term quantum hardware constraints [25–31].

As a representative benchmark for comparing classical and quantum reinforcement learning approaches, prior work has frequently considered the CartPole task, owing to its simplicity, low-dimensional state space, and suitability for assessing learning efficiency [28, 32–34]. Within this setting, a growing body of quantum reinforcement learning (QRL) research has explored parameterized quantum circuits (PQCs) as trainable components of the policy and value function, primarily to study learning behavior, parameter efficiency, and feasibility on near-term quantum hardware.

Several earlier studies have investigated PQC-based agents on CartPole and related control tasks without an explicit focus on real-time deployment nor any hardware implementation results. Chen et al., 2020. [25] implemented a value-based approach where a PQC computes the state-action value (Q) function based on deep Q-learning [35]. The agent would sample the action corresponding to the highest calculated Q-value at the quantum circuit output. Chen’s model represented the earliest PQC model functioning as value function approximator, which was later extended in Jerbi et al’s work as policy approximator [27]. Jerbi et al. [27] introduced the SOFTMAX-PQC model, in which a softmax policy is derived from expectation values of a multi-qubit PQC with trainable observable weights, input scaling parameters, and variational gate angles. The proposed models, based on classically hard yet trainable PQCs, were evaluated on standard OpenAI Gym environments including CartPole-v1, MountainCar, and Acrobot using a Q-learning algorithm, but did not consistently meet the solving conditions of the learning tasks. Skolik et al. [28] investigated PQC-based deep Q-learning agents on OpenAI Gym benchmarks including CartPole, focusing on architectural design choices such as data encoding strategies, readout observables, and circuit depth, and demonstrated that learning performance is highly sensitive to these design decisions. Hsu, Lin, and Wang [36] presented a comparative study of quantum and classical reinforcement learning on the CartPole task, using simulated parameterized quantum circuits trained with Proximal Policy Optimization and reporting competitive performance with fewer trainable parameters and training episodes relative to classical baselines. Collectively, these studies provide insight into the learning behavior and architectural considerations of PQC-based agents, but remain limited to simulation-based evaluation and do not address hardware execution constraints or real-time control considerations.

More recent studies have begun to address aspects of hardware execution that are relevant to real-time control. Hsiao et al. [37] investigated unentangled single- and multi-qubit PQC architectures trained with Proximal Policy Optimization (PPO), demonstrating successful learning on CartPole, Acrobot, and LunarLander environments and executing the trained policies on an IBM quantum processor, thereby addressing practical aspects of hardware inference relevant to real-time control, albeit without a systematic latency or stability analysis.

Among existing studies, Sun et al. [38] are most closely aligned with the focus of this work. They trained a variational quantum circuit policy using a model-based offline reinforcement learning approach, in which a dynamics model is learned from a fixed dataset of pre-collected physical CartPole environment interactions and subsequently used for policy optimization, and demonstrated its deployment in a real-time CartPole control experiment. Notably, their implementation relied on an eight-qubit quantum policy executed on embedded hardware via a Raspberry Pi-based quantum simulator to partially control a physical CartPole system. They further analyzed the latency constraints of cloud-based quantum execution, reporting action latencies exceeding three seconds when using standard IBM QPU access [38], which rendered such execution unsuitable for latency-sensitive control. Consequently, their results highlighted the need

to rely on simulator-based execution for real-time operation. As a result, realizing closed-loop CartPole control directly on a physical quantum processing unit—where the agent must simultaneously contend with hardware noise and execution latency—remains an open challenge.

In this paper, we study PQC-based reinforcement learning on CartPole with an explicit focus on the gap between simulation-only evaluations and latency- and noise-constrained deployment. Our goal is to assess how a minimal hybrid quantum–classical agent behaves (i) during training under shot-based gradient estimation, (ii) under different inference-time constraints such as control-loop rate and shot budget, and (iii) when executed through a low-latency hardware control path that approaches real-time feedback requirements.

We adopt an actor–critic policy-gradient baseline and augment it with a single-qubit variational circuit (five gates) adapted from [37] as the quantum component. We benchmark a fully classical agent against the hybrid agent on CartPole-v1 [39]. A central contribution is that the hybrid agent retains its sample-efficiency advantage not only under analytical (expectation-value) gradients but also when trained using the parameter-shift rule with finite-shot circuit evaluations.

We then move from training to deployment constraints by mapping the inference-time trade-off between control-loop rate and sampling precision. Concretely, we evaluate how balancing performance changes as the inference control frequency and per-action shot count are varied under a realistic noisy backend, thereby identifying the regimes in which the quantum policy remains stable versus those in which it fails. As part of the same sweep, we also vary the training control frequency to probe robustness under train–deploy mismatch; however, its effect is secondary compared to the inference-time constraints. Overall, the resulting performance maps are intended as practical guidance for future real-time CartPole demonstrations on quantum hardware, where the achievable control frequency and measurement budget are jointly limited by end-to-end latency.

Finally, we address the dominant bottleneck for hardware deployment—the latency of standard cloud and software stacks—by implementing a low-level inference pipeline that bypasses the high-level interface and directly programs the control and readout electronics. Using this approach, we demonstrate inference iteration rates up to 6.2 Hz on a superconducting QPU, enabling substantially faster closed-loop policy execution than is achievable via standard access paths.

The remainder of this paper is organized as follows: section 2 details basic CartPole benchmarking task, the actor-critic framework, the hybrid network architecture, and the specific experimental protocols for simulation and hardware inference. Section 3 presents the benchmarking results and the latency analysis, followed by a discussion of the implications for real-time quantum control in Section 4.

## 2 Methodology

### 2.1 The CartPole Environment

In the CartPole learning task, the objective is to stabilize an inverted pendulum mounted on a cart by applying discrete left or right forces at fixed control intervals, as illustrated in Fig. 1. An episode corresponds to a single interaction trajectory between the agent and the environment and terminates either when the pole exceeds a stability threshold or when a predefined maximum duration is reached. In this work, the maximum episode duration is set to correspond to 10 seconds in the environment.

Each episode is discretized into  $N_{\text{t-steps}}$  control steps determined by the control frequency  $f$ . The agent receives a reward of one per timestep, such that the maximum achievable return is 500 at the default control frequency of  $f = 50$  Hz, for example. At each timestep  $i$ , the environment provides a four-dimensional observation vector

$$s_i = (x_i, \dot{x}_i, \varphi_i, \dot{\varphi}_i),$$

encoding the cart position and velocity as well as the pole angle and angular velocity. The cart position and pole angle are bounded,

$$x_i \in [-2.4, 2.4], \quad \varphi_i \in [-0.418, 0.418] \text{ rad}, \quad (1)$$

while the velocity components  $\dot{x}_i$  and  $\dot{\varphi}_i$  are nominally unbounded. Aside from reaching the 10-second-mark, episodes terminate if the cart leaves the interval  $|x_i| > 2.4$  or the pole angle exceeds  $|\varphi_i| > 0.418$  radians. The learning agent is rewarded +1 for each time step the pole stays within a smaller bound  $|\varphi_i| > 0.2$  radians.

**2.1.1 Feature Selection** In our experiments we do not feed the full state  $s_i$  to the agent, but instead use a reduced three-dimensional feature vector

$$\tilde{s}_i = (\dot{x}_i, \varphi_i, \dot{\varphi}_i), \quad (2)$$

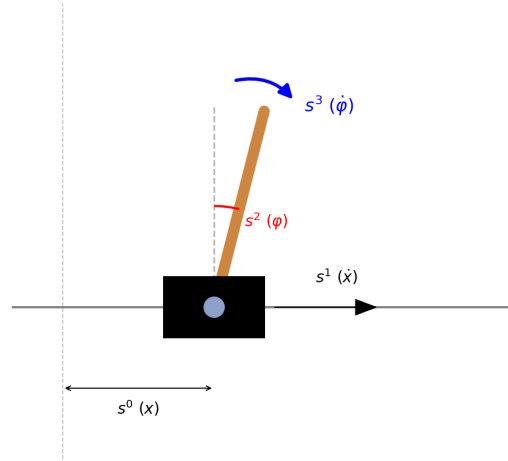


Figure 1: Schematic of the CartPole environment. The task consists of balancing the inverted pendulum mounted on the movable cart by applying discrete left or right forces. The observation states set  $\tilde{s} = [s^1, s^2, s^3, s^4]$  is described by the cart position  $x$  and velocity  $\dot{x}$ , as well as the pole angle  $\varphi$  and angular velocity  $\dot{\varphi}$  respectively.

obtained by discarding the cart position  $x_i$ . This reduction is motivated by the simple single-qubit design of the hybrid agent (elaborated more upon in Sec. 2.4): the encoding of the VQC maps  $\tilde{s}_i$  to a point on the Bloch sphere, which is effectively described by two real degrees of freedom (up to a global phase). Therefore, restricting the input state to three observables helps reduce the degeneracy of the state encoding. However, since the episodic termination criterion dictates a boundary on the cart position, the observable was kept track of and the episode was terminated whenever  $x_i$  did not lie within the allowed region.

## 2.2 The Actor-critic Method

In the CartPole environment, for each time-step  $t_i = i\Delta t$ , where  $\Delta t$  represents the duration of a single time step, the system state  $s_i$  is defined by the cart velocity  $\dot{x}$ , pole angle  $\varphi$ , and pole angular velocity  $\dot{\varphi}$ :

$$s_i = (\dot{x}(t_i), \varphi(t_i), \dot{\varphi}(t_i)) \quad (3)$$

The objective is to maximize the return. For a trajectory  $\tau = (s_0, a_0, s_1, a_1, \dots, s_T, a_T)$  of length  $T$ , the return is defined as the cumulative discounted reward:

$$R(\tau) = \sum_{i=0}^T \gamma^i r_i(s_i, a_i). \quad (4)$$

where  $\gamma$  is the discount rate. We implement the Actor-critic (AC) method with a policy gradient (PG) algorithm [40]. AC contains an actor that takes the states as input and outputs the probability distribution of the action, while the critic evaluates the value of the chosen action. The actor learns the policy  $\pi_\theta(a_i | s_i)$ , which governs the probability of selecting action  $a_i$  given state  $s_i$  [41]. To maximize performance, the policy parameter  $\theta$  is updated via gradient descent from a surrogate loss function that approximates the negative expected return:

$$\theta_{i+1} = \theta_i - \alpha \nabla L_{\text{actor}}(\theta_i) \quad (5)$$

Here,  $\alpha$  is the learning rate and the loss function for the actor is defined as

$$L_{\text{actor}}(s_i, \theta) = -\frac{1}{T} \sum_{i=0}^T \log(\pi_\theta(a_i | s_i)) \cdot A^{\pi_\theta}(s_i, a_i), \quad (6)$$

where  $A^{\pi_\theta}$  represents the advantage of the state-action pair at time-step  $i$ . In the Actor-Critic framework, the advantage is estimated using the Temporal Difference (TD) error:

$$A_t \approx \delta_t = r_t + \gamma V_\phi(s_{t+1}) - V_\phi(s_t) \quad (7)$$

**Algorithm 1** Episodic Actor-Critic with Policy Gradient

---

**Require:** Actor  $\pi_\theta$ , Critic  $V_\phi$ , Optimizers  $\text{Adam}_\theta, \text{Adam}_\phi$

**for** episode  $e = 1 \dots E$  **do**

$t \leftarrow 0, \tau \leftarrow \emptyset$ , Reset environment to  $s_0$

**while** not done and  $t < T_{max}$  **do**

Get Action and Value:  $a_t \sim \pi_\theta(\cdot | s_t), v_t \leftarrow V_\phi(s_t)$

Execute  $a_t$ , observe  $r_t, s_{t+1}, d_t$   $\triangleright d_t = 1$  if terminal

Store  $\tau \leftarrow (r_t, v_t, \log \pi(a_t | s_t), d_t)$

$t \leftarrow t + 1$

**end while**

Initialize Returns list  $D \leftarrow \emptyset$

$R_{next} \leftarrow V_\phi(s_t)$

**for**  $k = t - 1$  **down to** 0 **do**

$R_k \leftarrow r_k + \gamma \cdot R_{next} \cdot (1 - d_k)$

Insert  $R_k$  at start of  $D$

$R_{next} \leftarrow R_k$

**end for**

**Compute Advantage:**  $A_k = R_k - v_k$   $\triangleright$  Using stored  $v_k$

**Update Networks:**

$L_{actor} = -\frac{1}{T} \sum_{k=0}^T A_k \log \pi_\theta(a_k | s_k)$

$L_{critic} = \frac{1}{T} \sum_{k=0}^T H_\delta(R_k - v_k)$

$\theta \leftarrow \text{Adam}_\theta(\nabla_\theta L_{actor}); \phi \leftarrow \text{Adam}_\phi(\nabla_\phi L_{critic})$

**end for**

---

The state value function  $V_\phi(s_i)$ , parameterized by weights  $\phi$  and computed by the critic network, estimates the expected cumulative discounted reward from state  $s_i$ :

$$V_\phi(s_i) = \mathbb{E} \left[ \sum_{k=0}^{\infty} \gamma^k r_{i+k} \mid s_i \right]. \quad (8)$$

Traditional reinforcement learning methods often rely on lookup tables for value estimation; however, this approach is computationally expensive for large state-action spaces. Neural networks are often employed here to approximate these values efficiently, accommodating non-linearities [42]. The critic network is optimized to minimize the error between its prediction  $V_\phi(s_i)$  and the TD target  $y_i = r_i + \gamma V_\phi(s_{i+1})$ . We employ the Huber loss function to effectively handle outliers:

$$L_{critic} = \frac{1}{T} \sum_{i=0}^T H_\delta(y_i - V_\phi(s_i)) \quad (9)$$

where

$$H_\delta(e) = \begin{cases} 0.5e^2 & \text{if } |e| < \delta \\ \delta(|e| - 0.5\delta) & \text{otherwise.} \end{cases} \quad (10)$$

The reinforcement learning algorithm is summarized in Algorithm 1.

### 2.3 Classical Neural Network Model

As a classical baseline, we represent both the actor and the critic by separate fully connected neural networks. Each network takes the continuous state vector  $s_i$  as input and processes it through two hidden layers with 128 and 256 units, respectively. Both hidden layers use rectified linear unit (ReLU) activations to capture nonlinear dependencies in the state space. The actor and critic networks are shown in Figure

The actor network maps the input state to a vector of logits in  $\mathbb{R}^{|A|}$ , where  $|A| = 2$  is the number of discrete actions. These logits are passed through a softmax layer to obtain a categorical policy  $\pi_\theta(a_i | s_i)$  over actions. In contrast, the critic network has an identical hidden-layer structure but terminates in a single linear output neuron, producing a scalar estimate of the state value  $V_\phi(s_i)$ . The actor and critic do not share parameters, allowing each to specialize in policy representation and value estimation, respectively. 2.

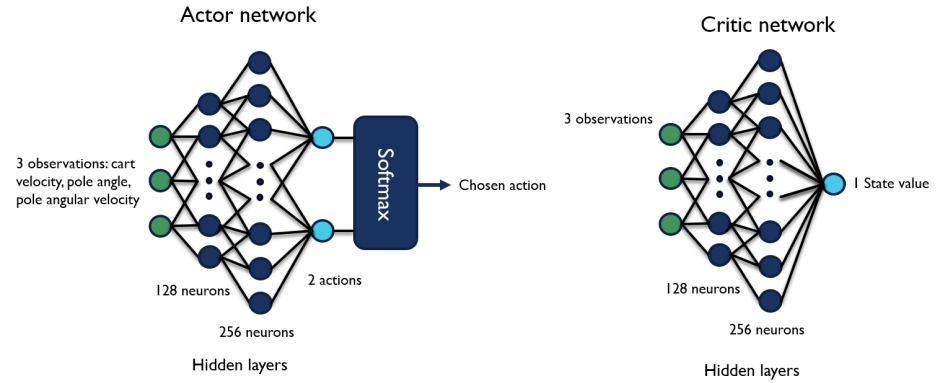


Figure 2: Classical actor network (left) and critic network (right) illustrations. Both networks share an identical internal structure consisting of an input layer for observations followed by two hidden layers of 128 and 256 neurons, respectively. The input layer received the raw observations. While the actor network contained the Softmax function to calculate the action probability distribution, the critic outputs a single state value judging how well the current environment states is. By comparing this value to actual reward, the agent determines whether the actor’s chosen action was better or worse than expected.

#### 2.4 Quantum-classical Hybrid Neural Network

The hybrid quantum-classical network architecture employs a single-qubit parameterized quantum circuit connected to classical, fully connected layers adapted from [37]. The quantum module begins with a Hadamard gate to create the  $|+\rangle$  state, followed by a three-rotation state-encoding sequence ( $R_z-R_y-R_z$ ) that maps the reduced CartPole observation vector (given in Sec. 2) onto the Bloch sphere, and concludes with a trainable  $R_x(\theta)$  rotation. The resulting expectation value of a Pauli- $Z$  measurement is copied to each input neuron of the downstream classical actor and critic networks, each consisting of a single hidden layer with 32 neurons and ReLU activation. The entirety of the hybrid quantum neural network reinforcement learning model for the CartPole task is illustrated in Figure 3.

We implement a variational quantum circuit (VQC) to leverage this high-dimensional space for encoding reinforcement learning states [43]. At each time step  $i$ , the reduced observable vector described in Sec. 2.1 is first preprocessed element-wise with the arctan function to further reduce degeneracy along each axis individually. This is indicated as  $\beta = \arctan(x_i, \dot{x}_i, \varphi_i, \dot{\varphi}_i)$  in Figure 3. The preprocessed states are then encoded into a quantum state  $|\psi(s_i)\rangle$  via a unitary embedding operator  $U(s_i)$ :

$$|\psi(s_i)\rangle = U(s_i)|0\rangle \quad (11)$$

where  $|0\rangle$  represents the initial quantum state. For this specific task, we utilize a single-qubit architecture. The embedding operator  $U(s_i)$  comprises a Hadamard gate to induce superposition, followed by rotation gates ( $R_z, R_y, R_z$ ).

$$U(s_i) = R_z(\beta_3)R_y(\beta_2)R_z(\beta_1)H. \quad (12)$$

Following encoding, the circuit applies a rotation gate around the X-axis  $R_x(\theta)$ , where  $\theta \in \mathbb{R}$  represents the trainable parameter whose initial value is controlled by the run-specific seed. The resulting quantum state  $|\psi(s_i, \theta)\rangle$  is measured via projection onto the Pauli-Z axis ( $\sigma_z$ ). The output of the VQC is given as follows:

$$f(s_i, \theta) = \langle 0|U^\dagger(s_i, \theta)M_{\sigma_z}U(s_i, \theta)|0\rangle. \quad (13)$$

The above expectation value can be simulated analytically or obtained as a statistical estimate by sampling the circuit  $N_{\text{shots}}$  times. As the system size grows, concerns of exponential concentration [44] rise for the latter approach, as exponentially many samples may be needed for the accurate estimation of the observable motivating a careful design of the circuit used.

The output  $f(s_i, \theta)$  is repeated 32 times and passed to a classical feedforward neural network (FNN), that outputs probabilities for each possible action. The FNN consists of a layer of 32 neurons outputting 2 logits, which is followed by a softmax activation function. The process of reusing PQC output has been reported by [37] to increase convergence speed of the learning agent

on CartPole benchmark. The critic outputs, as in the classical baseline, a single value. This architecture forms the basis for the training–inference compatibility study detailed in Section 2.5.2, where we evaluate the model’s robustness to the shot-noise and latency constraints inherent to the physical QPU. Finally, to enable gradient-based optimization of the quantum circuit parameters within the classical training loop, we utilize the parameter-shift rule. A detailed derivation of this method and its integration with standard backpropagation is provided in Appendix A.

### 2.5 Experiment Categories and Backends

In this work we consider three categories of experiments: (i) a noiseless benchmark comparing classical and hybrid quantum–classical agents, (ii) a training–inference compatibility study for the hybrid agent across different execution backends, control frequencies, and shot counts, and (iii) low–latency inference on a real quantum processor. All experiments use the CartPole-v1 environment with a maximum episode length corresponding 10 seconds.

**2.5.1 Noiseless Baseline: Classical vs. Hybrid Agents** The first set of experiments establishes a baseline comparison between the purely classical actor–critic agent with policy gradient described in Section 2.3 and two variants of the hybrid quantum–classical agent explained in Section 2.4 by utilizing the default control frequency of  $f_c = 50\text{Hz}$ . All agents are trained using the Qiskit BasicSimulator backend with 1024 shots.

For each model type (classical, hybrid with parameter–shift gradients, and hybrid with analytical gradients), we train an ensemble of 50 independent agents. Agents differ only by their random initialization: classical and quantum network parameters are drawn from separate random seeds, and episode-wise environment initial states are also randomized. This ensemble setting allows us to probe the robustness of convergence behaviour rather than a single representative run.

Episodes are capped at 500 time steps and training runs for at most 1500 episodes. As a success criterion we require that an agent achieves an average episodic return of 500 over 100 consecutive episodes, which corresponds to near–perfect balancing performance. Once this criterion is met, training for that agent is terminated and the corresponding network parameters are stored for subsequent analysis. In this noiseless setting the hybrid agents exhibit faster convergence to this success criterion than the classical baseline.

**2.5.2 Training–Inference Compatibility Study for the Hybrid Agent** The second group of experiments investigates the transferability of learned hybrid quantum–classical policies across different training and deployment condition combinations. This compatibility study systematically evaluates how agents trained at a given control frequency perform when deployed at different inference frequencies and shot budgets.

All training experiments in this study are performed using the Qiskit BasicSimulator backend, which provides finite-shot sampling without additional device noise. Expectation values required for gradient estimation are obtained using 4096 measurement shots per circuit execution, enabling stable parameter-shift gradients while remaining computationally feasible. Agents are trained at five discrete control frequencies,

$$f \in \{20, 25, 33, 50, 100\} \text{ Hz},$$

corresponding to time discretizations  $\tau = 1/f \in \{0.05, 0.04, 0.03, 0.02, 0.01\}$  seconds. To ensure that all agents solve an equivalent control task, the episode duration is fixed to 10 seconds of simulated time across all frequencies by setting the maximum number of time steps according to  $T_{\max} = 10/\tau$ . As a result, agents experience different numbers of decision points (e.g. 200 steps at 20 Hz versus 1000 steps at 100 Hz) while facing the same physical control objective.

For each training frequency, an ensemble of ten independent agents is trained using unique, deterministic random seeds to ensure reproducibility. Training proceeds for 500 episodes using the actor–critic algorithm with policy gradients. Both quantum circuit parameters and classical network weights are optimized using the Adam optimizer with a learning rate of  $\alpha = 0.05$  for both actor and critic ( $\beta_1 = 0.9$ ,  $\beta_2 = 0.999$ ). The hybrid architecture consists of a single-qubit variational circuit coupled to a classical neural network with 32 hidden units, as detailed in Section 2.4. Upon completion of training, the model weights including both quantum parameters and classical weights are saved for the subsequent compatibility evaluation.

The compatibility analysis evaluates each of the five training configurations across all inference frequencies, constructing a complete  $5 \times 5$  transfer matrix for each inference shot count. During inference, the policies are executed using shot counts of 128, 256, 512, and 1024 shots per circuit

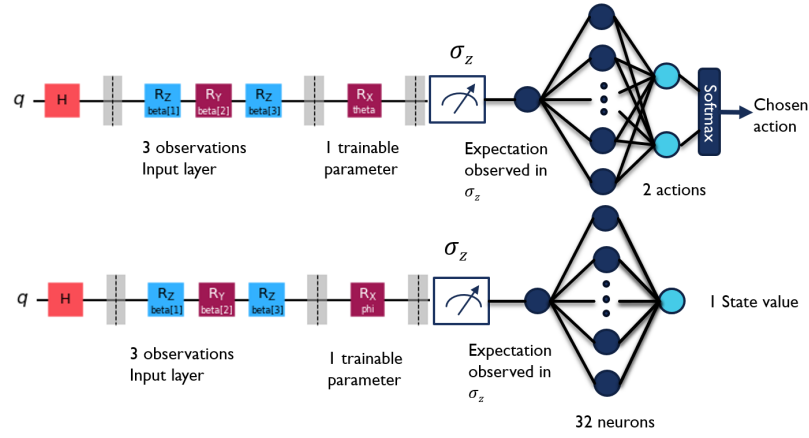


Figure 3: Hybrid quantum neural network for the actor (top) and critic (bottom). The functions of both actor and critic remain the same as its classical counterpart. The NN has been replaced by PQCs to approximate policy function (actor) and value function (critic). Each PQC output is copied 32 times before fully connected to two outputs (actor) and one output (critic). Soft is also used to output the final probability distribution.

execution, reflecting the execution time constraints typical of near-term quantum hardware. No further parameter updates are performed during inference and episode durations are again fixed to 10 seconds of simulated time by adjusting the timestep limit according to the inference frequency, enabling direct comparison of control performance across configurations. For each combination of training frequency, inference frequency, and shot count, 10 evaluation episodes are performed and the performance is quantified using mean duration.

This experiment subset enables a quantitative assessment of several deployment-relevant questions for PQC-based reinforcement learning: the extent to which policies potentially overfit to a specific control frequency, the impact of frequency mismatch on closed-loop stability, and, most importantly the sensitivity of policy performance to both reduced sampling precision inference control frequency.

*2.5.3 Quantum Hardware Implementation for Low-Latency Inference* The third set of experiments focuses on low-latency control on a real quantum processing unit. Here we no longer update the policy parameters; instead, we deploy a previously trained hybrid agent in pure inference mode and measure its control performance and iteration speed on hardware.

For these experiments we select an agent which has satisfied the stability criterion during training and demonstrated robust performance in the compatibility study when evaluated on the IQMFakeAdonis backend, which emulates the target device.

The selected agent is then executed on VTT Q5 using the optimized low-level control stack described in Section 2.7. Episode scores and timing statistics (iteration rate and throughput) are recorded for different shot counts, providing a direct measurement of how the learned policies perform and how close current hardware can come to the real-time control requirements of the CartPole task.

## 2.6 Training Details

For the training-inference compatibility studies, the training configurations explored a comprehensive parameter space:

- Gradient estimation: parameter-shift rule [45] for shot-based backends; analytical gradients via automatic differentiation for ExpVal backend
- Measurement shots per circuit execution:  $N_{\text{shots}} \in \{128, 256, 512, 1024\}$ ; analytical expectation values for ExpVal backend
- Control frequencies:  $f \in \{20, 25, 33, 50, 100\}$  Hz, corresponding to time discretization parameters  $\Delta t \in \{0.05, 0.04, 0.03, 0.02, 0.01\}$  seconds

For the optimization procedure employed the Adam optimizer [46] with separate learning rates for actor and critic networks. Quantum circuit parameters  $\theta$  and episode-wise environments were

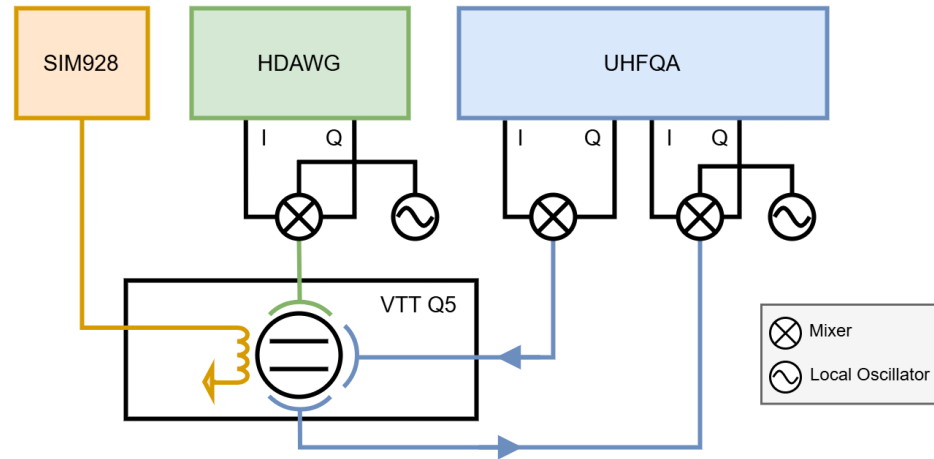


Figure 4: Experimental setup for measurements on Qubit 3 of the VTT Q5 device. The qubit flux bias is provided by an SRS SIM928 source (orange), which sets the qubit frequency and remains constant throughout the experiment. Microwave drive pulses are generated by the HDAWG (green), while readout pulses are produced by the UHFQA. Qubit drive pulses are implemented via frequency up-conversion, where narrow-band intermediate-frequency in-phase (I) and quadrature (Q) signals are mixed with a high-frequency local oscillator using an IQ mixer.

initialized using agent-specific random seeds, yielding distinct circuit and environment initializations for each agent and thereby promoting diverse training trajectories across the ensemble.

### 2.7 Low-latency Inference Configuration

We run our experiments on VTT Q5, a 5-qubit superconducting quantum computer developed by IQM and VTT. The qubits are flux-tunable and assume a star topology. The native gates consists of the single-qubit Phased- $RX$  (PRX) gate, the  $CZ$ -gate, and single-qubit measurements in the  $Z$ -basis. The PRX gate is defined as

$$PRX(\phi, \theta) = e^{-i(X \cos \phi + Y \sin \phi)\theta/2} \quad (14)$$

and enables arbitrary rotations around the  $X/Y$ -plane. The gate is implemented as a microwave pulse. Rotations around the  $Z$ -axis are achieved by virtual- $Z$  rotations [47], corresponding to phase shifts in the control electronics. The PRX gate is implemented as a Gaussian DRAG pulse [48] with a duration of 120 ns. The circuit in Figure 3 can be expressed by three PRX pulses

$$PRX(\theta, -\beta_1 - \beta_3) \quad PRX\left(\beta_2, \frac{\pi}{2} - \beta_1\right) \quad PRX\left(\frac{\pi}{2}, \frac{\pi}{2}\right). \quad (15)$$

The IQM quantum control stack (QCS) accepts Qiskit circuits as well as pulse sequences, defined in IQM’s pulse-level language, and compiles them to hardware instructions using the instrument drivers. For VTT Q5, an arbitrary waveform generator (AWG) from Zurich Instruments (HDAWG) is used to drive the qubits, which generates pulses at a sampling rate of 2.4 GSa/s. For readout, an ultra-high frequency quantum analyzer (UHFQA) is used, with a sampling rate of 1.8 GSa/s. Figure 4 shows the experimental setup. Both HDAWG and UHFQA are programmed in Zurich Instruments’ SeqC language, allowing precise playback of a sequence of microwave pulses on all channels.

To execute our parameterized circuit in Qiskit, we first bind the free gate parameters  $(s_i^0, s_i^1, s_i^2, \theta_i)$  and then transpile the circuit to native gates. The circuit is then submitted to the QCS and transformed into an intermediate representation (IR). The IR is translated into a sequence of pulses on each channel (e.g., qubit drive and flux bias). The parameters of each gate are translated to pulse parameters (e.g., amplitude and duration) determined by daily calibration (see Table 2 for reference values). In a final step, the waveform samples for each pulse and the SeqC code for the HDAWG and UHFQA are generated and uploaded to the devices. Finally, execution is triggered. After successful execution, the results are fetched from the UHFQA by the QCS and returned in Qiskit format to the user.

In our experiments utilizing the standard Qiskit software stack we found that the execution speed is limited by the re-compilation of SeqC code and upload of code and waveforms to the

devices upon circuit parameter changes. An average step frequency of 0.14 Hz for 512 shots (Table 1) was achieved. To speed up the execution, we bypass the QCS and connect directly to the Zurich Instrument devices. The execution on the Zurich Instrument devices is driven by a command table (CT). The CT consists of an indexed list, where each entry points to a waveform stored in memory and additional phase-shift and amplitude-scaling values for the IQ-components of the pulses. The SeqC code consists of triggers executing CT entries and idling instructions controlling the timing of the pulses for driving and measuring the qubit. For our parameterized circuit this timing is fixed. Therefore, the SeqC code does not require re-compilation and we can skip this expensive step. For each new set of parameters we therefore only upload new waveforms and an updated command table and trigger the execution. This simple but effective solution reduces the execution time significantly as shown in Table 1. To further speed up the execution we optimized the wait time between two shots. To ensure that the qubit is in the ground state at the beginning of the execution, a wait time  $\gg T_1$  is prepended to each circuit. The default on VTT Q5 is 398  $\mu\text{s}$ . Sweeping over the reset wait time we found 220  $\mu\text{s}$  to be optimal, shortening the execution time significantly while maintaining circuit fidelity (see Figure 9).

### 3 Results

Overall, our experiments show that (i) the single-qubit hybrid agent can solve CartPole with substantially fewer episodes than a classical actor–critic baseline under ideal simulation even with the use of parameter-shift, (ii) the average balancing duration during inference increases with  $f_{c,\text{inf}}$  but not necessarily with  $f_{c,\text{train}}$ , and (iii) low-level access to the quantum control stack yields over an order of magnitude reduction in iteration latency on real hardware while achieving successful inference test scores.

#### 3.1 Learning Convergence

We first compare learning dynamics of the classical and hybrid agents in expectation-value simulation (Figures 5). We then analyse training–inference compatibility across backends, shot counts, and control frequencies using a series of balancing duration matrices (Figures 6 and 7). Finally, we present real-hardware inference benchmarks on VTT’s IQM five-qubit superconducting QPU, including iteration rates and corresponding episode scores (Table 1, Figure 8).

Figure 5 shows the episode-wise return trajectories and the average episode counts required to solve the task for the hybrid agent (with both analytical and parameter-shift gradient estimation) and for the fully classical agent. Results are averaged over 50 independently seeded runs of 500 episodes at the CartPole-v1 default control frequency of  $f = 50$  Hz. The hybrid agent trained with analytical gradients solves the task in the fewest episodes and maintains the most stable performance thereafter. Both hybrid variants converge significantly faster than the classical baseline, as shown in Fig. 5b.

#### 3.2 Effects of Control Frequency and Shot Count for Real-Time Inference

The second experiment category quantifies how hybrid policies behave under deployment constraints that may differ from training. This serves two roles in this work. First, it guides the choice of training configuration and inference settings used for the real-QPU experiments in Section 3.3. Second, it provides concrete parameter-regime guidance for future real-time demonstration consideration, where the achievable control frequency and inference shot budget are jointly limited by latency. Increasing the control frequency simultaneously increases the number of decision points per episode, while increasing the shot count improves estimation accuracy at the cost of execution latency. As a result, policy performance at inference time is governed by a trade-off between temporal resolution and measurement precision.

Motivated by this trade-off, we systematically explore how policies trained at different control frequencies perform when evaluated across a range of inference-time frequencies and shot budgets. All agents are trained using the Qiskit `BasicSimulator` backend under pure statevector with 4096 shots, while inference is carried out with varying control frequencies and shot counts on the `FakeAdonis` backend with a noise model that emulates the target QPU of the VTT Q5. This empirical study is designed to identify training–inference combinations that yield reliable control performance under realistic execution constraints, and to assess whether policies trained at higher control frequencies—which offer finer temporal resolution during training—exhibit increased sensitivity to finite-shot and device-level noise during deployment.

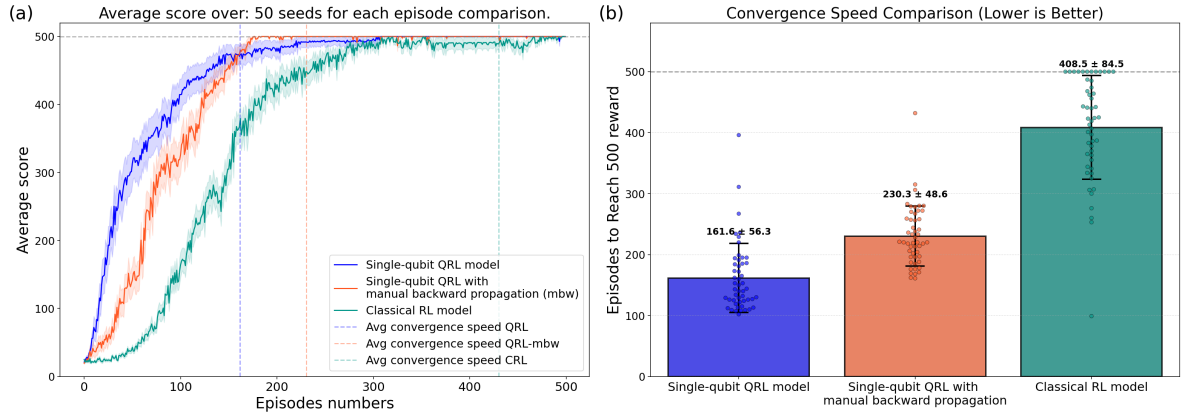


Figure 5: Average reward scores over 50 runs (5a). The single-qubit QRL model (blue) achieves the maximum reward threshold significantly faster than the Classical RL baseline (green), validating the higher sample efficiency observed in simulation. The orange curve represented the same QRL model with manual backward propagation process implemented. The dashed lines show the average episodes taken to solve the CartPole task. Average episode counts needed for the single-qubit QRL and classical RL models to reach the success criterion of 100 consecutive perfect episodes (5b). The Single-Qubit model (blue) demonstrates a 2.7x improvement in sample efficiency ( $161.6 \pm 56.3$  episodes) compared to the Classical model ( $429.4 \pm 117.9$  episodes) under ideal simulation conditions. Each dot represent the episode number when the models solve the task at different seed.

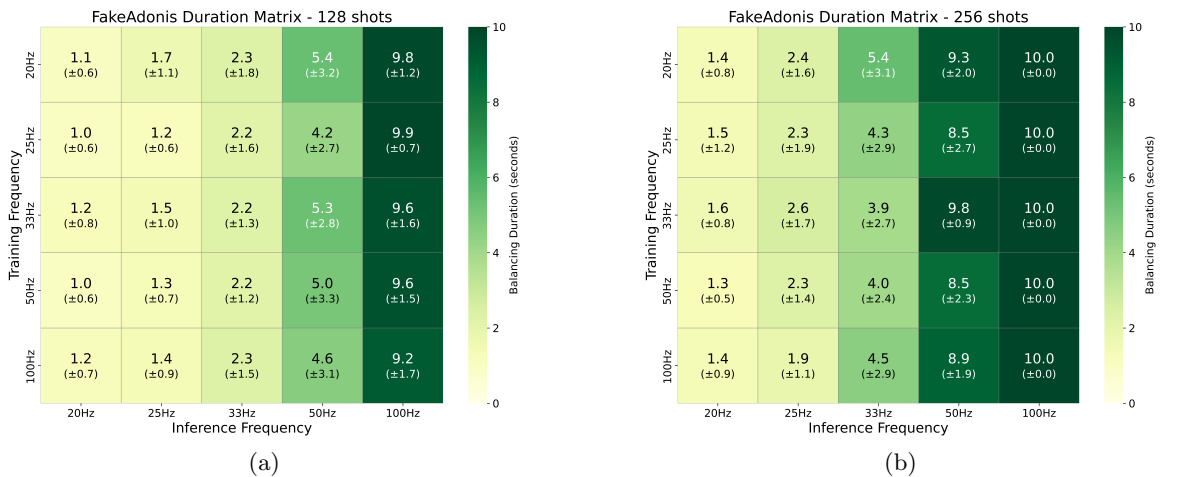


Figure 6: FakeAdonis duration matrices comparing 128 shots (a) and 256 shots (b). The heatmaps show mean balancing duration in seconds ( $\pm$  standard deviation) across different training and inference frequency combinations.

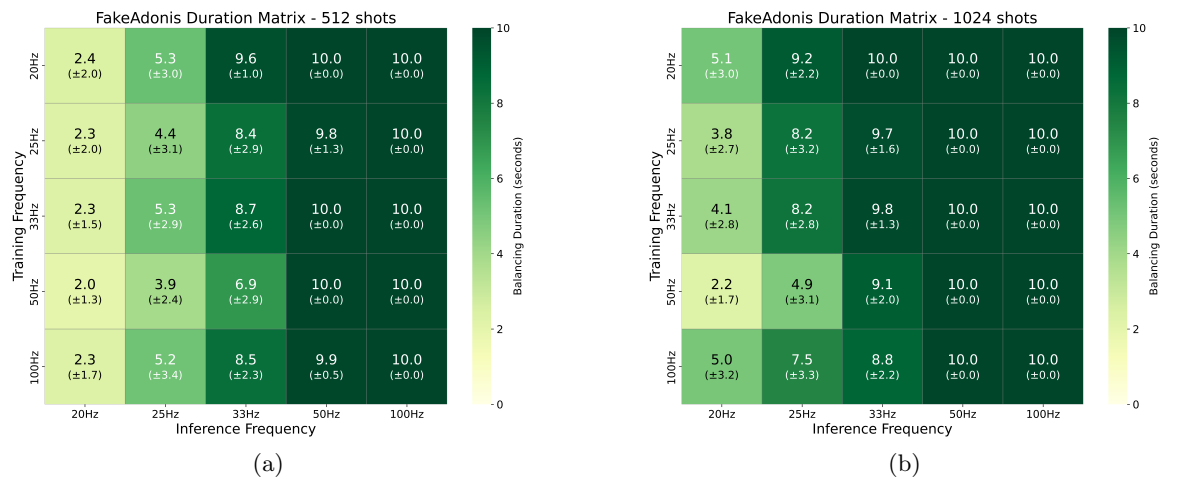


Figure 7: FakeAdonis duration matrices comparing 512 shots (a) and 1024 shots (b). Higher shot counts provide more stable quantum measurements, resulting in improved balancing performance and reduced variance across training–inference frequency combinations.

### 3.3 Low-latency Inference on a Real QPU

We next benchmark inference-only execution of a trained hybrid policy on VTT Q5 and quantify the latency benefit of bypassing the standard software stack. We compare the default IQM execution path against the low-level inference pipeline explained in Sec. 2.7 that directly drives the control and readout electronics.

Table 1 reports the average iteration rates (policy evaluations per second) for shot counts  $N_{\text{shots}} \in \{128, 256, 512, 1024\}$ . The standard IQM stack achieves  $\approx 0.14$  iter/s across regardless of shot count, whereas the low-level path reaches 6.23, 5.62, 4.28, and 2.71 iter/s, corresponding to speedups of  $43.3\times$ ,  $39.3\times$ ,  $30.1\times$ , and  $18.8\times$ , respectively.

Figure 8 summarizes the latency–performance trade-off. As expected, increasing the shot count reduces the iteration rate but improves control performance: average episode scores increase from  $\approx 143$  (128 shots) and  $\approx 166$  (256 shots) to  $\approx 474$  (512 shots), reaching perfect performance (500) at 1024 shots. These hardware runs use an inference control frequency of  $f_{c,\text{inf}} = 50$  Hz in a simulated, offline CartPole loop, and no readout error mitigation is applied. We emphasize that this operating point differs from the inference regimes identified as near-perfect in the duration-matrix study (which favored higher  $f_{c,\text{inf}}$  and/or larger shot budgets under the FakeAdonis model); as such, the absolute episode scores here should be interpreted as a conservative hardware demonstration under non-ideal inference conditions. Together, the results show that low-level execution enables order-of-magnitude faster closed-loop inference on hardware while preserving high CartPole performance when the shot budget is sufficiently large in the case of no readout mitigation.

Shots	IQM stack (iter/s)	Low-level (iter/s)	Speedup
128	0.144 ( $\pm 0.001$ )	6.23 ( $\pm 0.01$ )	<b>43.3</b> $\times$
256	0.143 ( $\pm 0.001$ )	5.62 ( $\pm 0.00$ )	<b>39.3</b> $\times$
512	0.142 ( $\pm 0.001$ )	4.28 ( $\pm 0.01$ )	<b>30.1</b> $\times$
1024	0.144 ( $\pm 0.002$ )	2.71 ( $\pm 0.01$ )	<b>18.8</b> $\times$

Table 1: Average iteration speeds for the IQM software stack and low-level inference at different shot counts, including computed speedups.

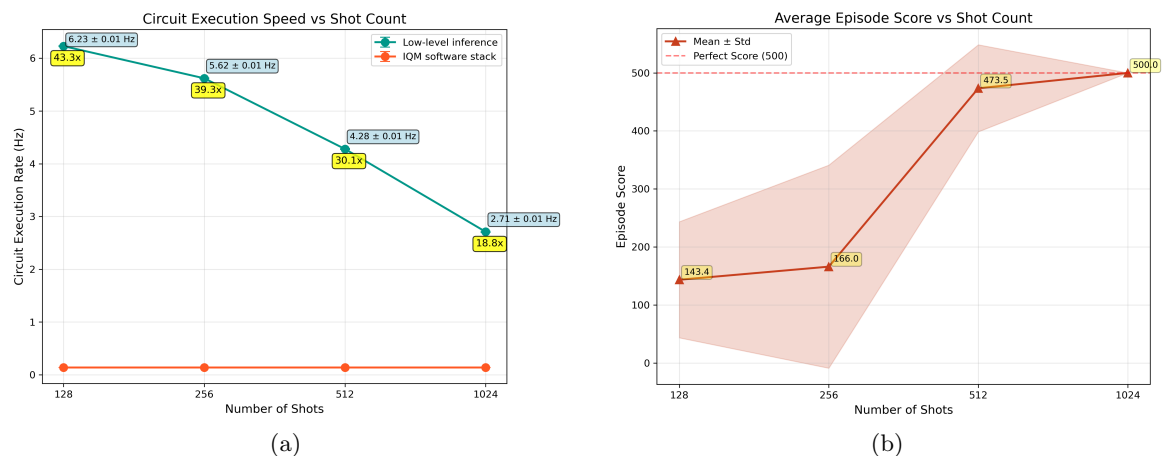


Figure 8: Average iteration rate and throughput (a) and corresponding inference-time episode scores (b) for shot counts of 128, 256, 512, and 1024. Error bars represent the standard deviation across five runs of ten episodes (a) and ten evaluation episodes (b). The red line at 500 points in panel (b) indicates perfect CartPole-v1 performance.

## 4 Discussion

In this work we have combined model-level, simulational, and hardware-level investigations to assess whether a minimal hybrid quantum–classical agent can (i) learn CartPole faster than a standard classical baseline, (ii) map out how performance depends on mismatches between training and deployment conditions across quantum backends and control frequencies, and (iii) be executed fast enough on current NISQ hardware to approach real-time control.

On the learning side, our expectation–value simulations show that a single-qubit hybrid agent with the encoding and feature set used in this work can solve CartPole in substantially fewer episodes than a comparable classical actor–critic network (Figures 5). This is in line with results

reported in another work [37]. This advantage persists even when gradients are estimated via the parameter-shift rule, albeit with slightly slower convergence than in the fully analytical setting. Given that CartPole is a low-dimensional, well-understood benchmark, these results do not constitute a quantum speed-up in the complexity-theoretic sense, but they do indicate that parametrized single-qubit circuits can act as effective nonlinear function approximators within RL loops when paired with the chosen encoding and lightweight classical post-processing.

From the duration matrices in Figures 6 and 7, both the inference-time control frequency  $f_{c,\text{inf}}$  and the inference shot budget  $N_{\text{shots},\text{inf}}$  have a strong, expected impact on the average balancing duration: faster closed-loop updates and more precise (higher-shot) expectation estimates generally improve stability and reduce variability. A particularly clear reference point is  $f_{c,\text{inf}} = 100$  Hz, where all tested shot counts (128–1024) achieve mean balancing durations very close to the 10 s episode limit and often reach the limit, largely independent of training frequency. Moving to lower inference frequencies, the shot count increasingly determines where stable control becomes feasible: increasing  $N_{\text{shots},\text{inf}}$  shifts the onset of near-perfect performance to lower  $f_{c,\text{inf}}$  (i.e., configurations that require 100 Hz at low shot budgets can succeed already around 50 Hz, and in some cases 33 Hz, when the shot count is increased). Notably, these results are obtained without applying readout error mitigation, so improved performance—especially in the lower-frequency / lower-shot regimes—would be expected with standard mitigation techniques. Finally, across the full sweep we observe no consistent dependence on the training control frequency  $f_{c,\text{train}}$ : for a fixed inference configuration ( $f_{c,\text{inf}}, N_{\text{shots},\text{inf}}$ ) the inference balancing durations remain broadly similar across all  $f_{c,\text{train}}$ , suggesting that deployment is governed primarily by inference-time constraints rather than the control frequency used during training.

Our hardware experiments on VTT Q5 address the practical question of whether such learned quantum policies can, in principle, be executed quickly enough for feedback control. By bypassing the high-level quantum control stack and directly programming the Zurich Instruments AWG and readout electronics via command tables, we achieve more than an order-of-magnitude improvement in iteration rate compared to the standard IQM stack (Table 1). The side-by-side timing and performance results in Figure 8 show that this low-level execution path maintains high CartPole scores while substantially reducing latency, yielding iteration rates in the range of 2.7–6.2 Hz depending on the shot count. Future work could explore more advanced sampling schemes. For example, active reset after the final measurement can reduce the inter-shot wait time significantly. Another simpler approach is the restless measurement scheme [49] where qubits are not reset between shots. However, the drawback of this approach is the requirement to make the circuit invariant with respect to the initial state being either  $|0\rangle$  or  $|1\rangle$ . Finally, the control electronics could be updated to the latest generation of devices or replaced by custom made instruments which support more granular control of drive and readout and reduced latencies.

Some limitations of our study point to natural directions for future work. First, all experiments are conducted on a single-qubit architecture without entanglement; extending the analysis to few-qubit ansätze would allow us to probe how the observed learning-speed trends and compatibility patterns scale with circuit size and the number of trainable parameters. In addition, one could explore ansätze whose hardware-level implementation would be independent of the discrete initial state ( $|0\rangle$  or  $|1\rangle$ ), so that the state would not necessarily require a reset after each shot. Such designs could offer further speedups, but they impose nontrivial structural constraints on the circuit, are very likely to reduce degrees of freedom within the state, and potentially become increasingly challenging to realize as the number of qubits grows.

On the hardware side, our results suggest concrete performance targets for quantum devices aimed at control applications. Closing the remaining gap between our current multi-hertz iteration rates and the tens-of-hertz regime required for real-time feedback would enable not only CartPole control in the lab, but also more ambitious demonstrations.

## 5 Conclusion

This work addresses the gap between theoretical quantum reinforcement learning and physical deployment by presenting an end-to-end investigation of a hybrid agent on the CartPole benchmark. We demonstrated that a minimal single-qubit model acts as a sample-efficient policy, solving the environment in significantly fewer episodes than a classical baseline even when trained under realistic parameter-shift gradients. Evidently, our hardware experiments quantified the latency bottlenecks inherent to standard cloud-access models. By bypassing the high-level software stack and programming the control electronics directly, we achieved inference rates of over 6 Hz—a speedup of more than 40x compared to standard execution. These results, combined with our analysis of the trade-offs between shot budget and control frequency, outline a roadmap for turning

small-scale quantum RL demonstrations into practical, closed-loop quantum controllers where latency and precision must be strictly balanced.

## References

- [1] Maria Schuld, Ilya Sinayskiy, and Francesco Petruccione. “An introduction to quantum machine learning”. In: *Contemporary Physics* 56.2 (2015), pp. 172–185.
- [2] Jarrod R McClean et al. “The theory of variational hybrid quantum-classical algorithms”. In: *New Journal of Physics* 18.2 (2016), p. 023023.
- [3] Jacob Biamonte et al. “Quantum machine learning”. In: *Nature* 549.7671 (2017), pp. 195–202.
- [4] Yunchao Liu, Srinivasan Arunachalam, and Kristan Temme. “A rigorous and robust quantum speed-up in supervised machine learning”. In: *Nature Physics* 17.9 (2021), pp. 1013–1017.
- [5] Casper Gyurik and Vedran Dunjko. “Exponential separations between classical and quantum learners”. In: *arXiv preprint arXiv:2306.16028* (2023).
- [6] John Preskill. “Quantum computing in the NISQ era and beyond”. In: *Quantum* 2 (2018), p. 79.
- [7] Marco Cerezo et al. “Variational quantum algorithms”. In: *Nature Reviews Physics* 3.9 (2021), pp. 625–644.
- [8] Adam Callison and Nicholas Chancellor. “Hybrid quantum-classical algorithms in the noisy intermediate-scale quantum era and beyond”. In: *Physical Review A* 106.1 (2022), p. 010101.
- [9] Marcello Benedetti et al. “Parameterized quantum circuits as machine learning models”. In: *Quantum science and technology* 4.4 (2019), p. 043001.
- [10] Maria Schuld and Nathan Killoran. “Quantum machine learning in feature Hilbert spaces”. In: *Physical review letters* 122.4 (2019), p. 040504.
- [11] Jemin Hwangbo et al. “Learning agile and dynamic motor skills for legged robots”. In: *Science Robotics* 4.26 (2019), eaau5872.
- [12] Jie Tan et al. “Sim-to-real: Learning agile locomotion for quadruped robots”. In: *arXiv preprint arXiv:1804.10332* (2018).
- [13] Elia Kaufmann et al. “Champion-level drone racing using deep reinforcement learning”. In: *Nature* 620.7976 (2023), pp. 982–987.
- [14] Xue Bin Peng et al. “Learning agile robotic locomotion skills by imitating animals”. In: *arXiv preprint arXiv:2004.00784* (2020).
- [15] Nate Kohl and Peter Stone. “Policy gradient reinforcement learning for fast quadrupedal locomotion”. In: *IEEE International Conference on Robotics and Automation, 2004. Proceedings. ICRA '04. 2004*. Vol. 3. IEEE. 2004, pp. 2619–2624.
- [16] David Silver et al. “A general reinforcement learning algorithm that masters chess, shogi, and Go through self-play”. In: *Science* 362.6419 (2018), pp. 1140–1144. DOI: [10.1126/science.aar6404](https://doi.org/10.1126/science.aar6404).
- [17] Oriol Vinyals et al. “Grandmaster level in StarCraft II using multi-agent reinforcement learning”. en. In: *Nature* 575.7782 (Nov. 2019), pp. 350–354.
- [18] Tingguang Li et al. “Learning Terrain-Adaptive Locomotion with Agile Behaviors by Imitating Animals”. In: *2023 IEEE/RSJ International Conference on Intelligent Robots and Systems (IROS)*. 2023, pp. 339–345. DOI: [10.1109/IROS55552.2023.10342271](https://doi.org/10.1109/IROS55552.2023.10342271).
- [19] Daoyi Dong et al. “Quantum Reinforcement Learning”. In: *IEEE Transactions on Systems, Man, and Cybernetics, Part B (Cybernetics)* 38.5 (2008), pp. 1207–1220. DOI: [10.1109/TSMCB.2008.925743](https://doi.org/10.1109/TSMCB.2008.925743).
- [20] Vedran Dunjko, Jacob M Taylor, and Hans J Briegel. “Quantum-enhanced machine learning”. In: *Physical review letters* 117.13 (2016), p. 130501.
- [21] Valeria Saggio et al. “Experimental quantum speed-up in reinforcement learning agents”. In: *Nature* 591.7849 (2021), pp. 229–233.
- [22] Giuseppe Davide Paparo et al. “Quantum speedup for active learning agents”. In: *Physical Review X* 4.3 (2014), p. 031002.
- [23] Arne Hamann, Vedran Dunjko, and Sabine Wölk. “Quantum-accessible reinforcement learning beyond strictly epochal environments”. In: *Quantum Machine Intelligence* 3.2 (2021), p. 22.

- [24] Daoyi Dong et al. “Robust quantum-inspired reinforcement learning for robot navigation”. In: *IEEE/ASME transactions on mechatronics* 17.1 (2010), pp. 86–97.
- [25] Samuel Yen-Chi Chen et al. “Variational quantum circuits for deep reinforcement learning”. In: *IEEE access* 8 (2020), pp. 141007–141024.
- [26] Owen Lockwood and Mei Si. “Reinforcement learning with quantum variational circuit”. In: *Proceedings of the AAAI conference on artificial intelligence and interactive digital entertainment*. Vol. 16. 1. 2020, pp. 245–251.
- [27] Sofiene Jerbi et al. “Parametrized quantum policies for reinforcement learning”. In: *Advances in Neural Information Processing Systems* 34 (2021), pp. 28362–28375.
- [28] Andrea Skolik, Sofiene Jerbi, and Vedran Dunjko. “Quantum agents in the gym: a variational quantum algorithm for deep q-learning”. In: *Quantum* 6 (2022), p. 720.
- [29] Qingfeng Lan. “Variational quantum soft actor-critic”. In: *arXiv preprint arXiv:2112.11921* (2021).
- [30] Samuel Yen-Chi Chen et al. “Variational quantum reinforcement learning via evolutionary optimization”. In: *Machine Learning: Science and Technology* 3.1 (2022), p. 015025.
- [31] Won Joon Yun et al. “Quantum multi-agent reinforcement learning via variational quantum circuit design”. In: *2022 IEEE 42nd International Conference on Distributed Computing Systems (ICDCS)*. IEEE, 2022, pp. 1332–1335.
- [32] Martin Riedmiller. “Neural Fitted Q Iteration – First Experiences with a Data Efficient Neural Reinforcement Learning Method”. In: *Proceedings of the Sixteenth European Conference on Machine Learning*. Vol. 3720. Lecture Notes in Computer Science. Springer, 2005, pp. 317–328.
- [33] Shlomo Geva and Joaquín Sitte. “A Cartpole Experiment Benchmark for Trainable Controllers”. In: *IEEE Control Systems Magazine* 13.5 (1993), pp. 40–51. DOI: [10.1109/37.236324](https://doi.org/10.1109/37.236324).
- [34] Owen Lockwood and Mei Si. “Reinforcement Learning with Quantum Variational Circuits”. In: *Proceedings of the AAAI Conference on Artificial Intelligence and Interactive Digital Entertainment (AIIDE)*. 2020.
- [35] Volodymyr Mnih et al. “Playing atari with deep reinforcement learning”. In: *arXiv preprint arXiv:1312.5602* (2013).
- [36] Hong-Chang Hsu, Yi-Hsiang Lin, and Yu-Jen Wang. “A Comparative Study on Quantum and Classical Reinforcement Learning for the CartPole Task”. In: *IFTToMM International Conference on Mechanisms, Transmissions and Applications*. Springer, 2025, pp. 261–269.
- [37] Jen-Yueh Hsiao et al. “Unentangled quantum reinforcement learning agents in the OpenAI Gym”. In: (Mar. 2022). arXiv: [2203.14348](https://arxiv.org/abs/2203.14348) [[quant-ph](https://arxiv.org/abs/2203.14348)].
- [38] Yize Sun et al. “First Experience with Real-Time Control Using Simulated VQC-Based Quantum Policies”. In: *arXiv preprint arXiv:2508.01690* (2025).
- [39] Greg Brockman et al. “OpenAI Gym”. In: (June 2016). arXiv: [1606.01540](https://arxiv.org/abs/1606.01540) [[cs.LG](https://arxiv.org/abs/1606.01540)].
- [40] Richard S Sutton et al. “Policy gradient methods for reinforcement learning with function approximation”. In: *Advances in neural information processing systems* 12 (1999).
- [41] Richard S Sutton and Andrew G Barto. *Reinforcement Learning*. en. Adaptive Computation and Machine Learning series. Cambridge, MA: Bradford Books, Feb. 1998.
- [42] Sardor Israilov et al. “Reinforcement learning approach to control an inverted pendulum: A general framework for educational purposes”. en. In: *PLoS One* 18.2 (Feb. 2023), e0280071.
- [43] M Cerezo et al. “Variational quantum algorithms”. en. In: *Nat. Rev. Phys.* 3.9 (Aug. 2021), pp. 625–644.
- [44] Martin Larocca et al. “Barren plateaus in variational quantum computing”. In: *Nature Reviews Physics* (2025), pp. 1–16.
- [45] Maria Schuld et al. “Evaluating analytic gradients on quantum hardware”. In: *Physical Review A* 99.3 (2019), p. 032331.
- [46] Diederik P Kingma and Jimmy Ba. “Adam: A method for stochastic optimization”. In: (Dec. 2014). arXiv: [1412.6980](https://arxiv.org/abs/1412.6980) [[cs.LG](https://arxiv.org/abs/1412.6980)].

- [47] David C. McKay et al. “Efficient Z gates for quantum computing”. In: *Physical Review A* 96 (2016), p. 022330. URL: <https://api.semanticscholar.org/CorpusID:119339298>.
- [48] F. Motzoi et al. “Simple Pulses for Elimination of Leakage in Weakly Nonlinear Qubits”. In: *Phys. Rev. Lett.* 103 (11 2009), p. 110501. DOI: [10.1103/PhysRevLett.103.110501](https://doi.org/10.1103/PhysRevLett.103.110501). URL: <https://link.aps.org/doi/10.1103/PhysRevLett.103.110501>.
- [49] M. Werninghaus, D.J. Egger, and S. Filipp. “High-Speed Calibration and Characterization of Superconducting Quantum Processors without Qubit Reset”. In: *PRX Quantum* 2.2 (May 2021). ISSN: 2691-3399. DOI: [10.1103/prxquantum.2.020324](https://doi.org/10.1103/prxquantum.2.020324). URL: <http://dx.doi.org/10.1103/PRXQuantum.2.020324>.
- [50] David E Rumelhart, Geoffrey E Hinton, and Ronald J Williams. “Learning representations by back-propagating errors”. In: *nature* 323.6088 (1986), pp. 533–536.
- [51] Ali Javadi-Abhari et al. “Quantum computing with Qiskit”. In: *arXiv preprint arXiv:2405.08810* (2024).
- [52] Ville Bergholm et al. “Pennylane: Automatic differentiation of hybrid quantum-classical computations”. In: *arXiv preprint arXiv:1811.04968* (2018).
- [53] Adam Paszke et al. “Pytorch: An imperative style, high-performance deep learning library”. In: *Advances in neural information processing systems* 32 (2019).
- [54] David Wierichs et al. “General parameter-shift rules for quantum gradients”. In: *Quantum* 6 (2022), p. 677.

### Acknowledgments

J.Q.Q. and P.W. acknowledges the financial support of the Quantum Technology Future Science Platform - CSIRO.

### Author contributions

N.T.T.N.: Conceptualization, Methodology (lead on hybrid quantum-classical architecture and single-qubit algorithm design), Software (development of RL agents and simulation environment), Formal analysis (simulation and compatibility studies between QRL and CRL models), Writing – original draft.

V.M: Conceptualization, Methodology (experiments on the training frequency and inference frequency), Software (experiments on inference), Formal analysis (simulation and compatibility studies between QRL and CRL models), Writing – original draft.

J.J: Methodology (hardware setup on VTT Q5), Software (VTT Q5 control stack), Formal analysis (circuit execution speed and shot count), Writing – original draft.

T.-F.L.: Supervision, Resources, Writing – review & editing. J.Q.Q.: Conceptualization, Supervision, Project administration, Funding acquisition, Writing – review & editing.

### Data availability

The data supporting the plots can be found at [10.5281/zenodo.18994218](https://zenodo.org/record/18994218). Source code and model weights are available upon reasonable request.

## A Gradient Computation

Backpropagation is a fundamental technique in training machine learning models, in which trainable parameters are iteratively updated to minimize a loss function [50]. When training on quantum simulators—such as Qiskit [51] or PennyLane [52]—this process is automated via seamless integration with PyTorch’s automatic differentiation library [53]. However, transitioning to physical quantum hardware disrupts this workflow. The Quantum Processing Unit (QPU) operates as an external execution environment outside the scope of the classical computational graph. Because the internal operations on the remote QPU are not tracked by PyTorch, and the quantum states collapse upon measurement, automatic gradient computation is rendered impossible.

Consequently, when training on a Noisy Intermediate-Scale Quantum (NISQ) device, the quantum parameters  $\theta$  are effectively decoupled from the classical automatic differentiation engine. To address this, the gradients for the quantum variational circuit must be calculated separately and bridged with the classical neural network. During the backward propagation step, the gradient of the loss function with respect to the trainable parameters  $\theta$ , denoted as  $\nabla L(\theta)$ , is required for the optimization algorithm (e.g., Adam). By applying the chain rule, this gradient can be expressed as:

$$\nabla L(\theta) = \frac{\partial L_{actor}}{\partial \theta} = \frac{\partial L_{actor}}{\partial f(s_i, \theta)} \cdot \frac{\partial f(s_i, \theta)}{\partial \theta} \quad (16)$$

Here, the term  $\frac{\partial L_{actor}}{\partial f(s_i, \theta)}$  represents the gradient of the loss function with respect to the quantum circuit’s output. Since  $f(s_i, \theta)$  serves as the input to the subsequent classical layers, this term can be computed using standard backpropagation via PyTorch. The second term,  $\frac{\partial f(s_i, \theta)}{\partial \theta}$ , represents the gradient of the quantum circuit output with respect to its own parameters. This is typically calculated using the parameter-shift rule [54]:

$$\frac{\partial f(s_i, \theta)}{\partial \theta} = \frac{1}{2} \left[ f\left(s_i, \theta + \frac{\pi}{2}\right) - f\left(s_i, \theta - \frac{\pi}{2}\right) \right] \quad (17)$$

This approach allows for the analytical calculation of gradients by executing additional circuit evaluations with shifted parameters on the physical hardware. These values are then fed back into the classical optimizer to update the model weights.

## B Additional Experiment Details

Parameter	Value
Drive $\omega_d/2\pi$ (GHz)	4.211
Drive duration (ns)	120
Readout frequency $\omega_{RO}/2\pi$ (GHz)	6.157
Readout duration ( $\mu$ s)	1
Reset wait between shots ( $\mu$ s)	398
$T_1$ -time ( $\mu$ s)	$22.94 \pm 2.03$
$T_2^*$ -time ( $\mu$ s)	$15.68 \pm 2.09$
$T_2$ -time ( $\mu$ s)	$26.19 \pm 4.92$
Single-qubit RB (%)	$99.76 \pm 0.01$
Single-shot readout fidelity (%)	95.45
Single-shot readout 0-1 error (%)	2.95
Single-shot readout 0-1 error (%)	6.15

Table 2: Qubit parameters, coherence times and gate fidelities as well as circuit execution details.

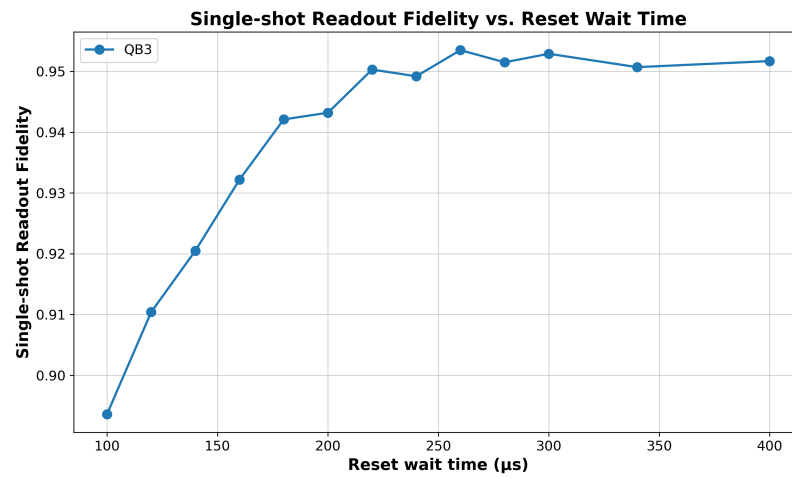


Figure 9: Single-shot readout fidelity as a function of reset wait time ( $\mu\text{s}$ ) for qubit 3 on VTT Q5. The reset wait time is the time between two shots to ensure that the qubit relaxes to the ground state. For each wait time 40,000 shots were executed.